Important Notice to Authors

<div style="border: 1px solid red; color: red;">

No further publication processing will occur until we receive your response to this proof.

</div>

Attached is a PDF proof of your forthcoming article in PRB. Your article has 9 pages and the Accession Code is **BS13965**.

Please note that as part of the production process, APS converts all articles, regardless of their original source, into standardized XML that in turn is used to create the PDF and online versions of the article as well as to populate third-party systems such as Portico, Crossref, and Web of Science. We share our authors' high expectations for the fidelity of the conversion into XML and for the accuracy and appearance of the final, formatted PDF. This process works exceptionally well for the vast majority of articles; however, please check carefully all key elements of your PDF proof, particularly any equations or tables.

Figures submitted electronically as separate files containing color appear in color in the online journal. However, all figures will appear as grayscale images in the print journal unless the color figure charges have been paid in advance, in accordance with our policy for color in print (https://journals.aps.org/authors/color-figures-print).

Specific Questions and Comments to Address for This Paper

  1 Supply page number in Refs. [1,2]
  2 Supply additional information (unpublished, private communication)?.
  3 Please update arXiv Ref. [8] if possible.
  4 Update reference.
FQ: This funding provider could not be uniquely identified during our search of the FundRef registry (or no Contract or Grant number was detected). Please check information and amend if incomplete or incorrect.
  Q: This reference could not be uniquely identified due to incomplete information or improper format. Please check all information and amend if applicable.

ORCIDs: Please follow any ORCID links (⬤) after the author names and verify that they point to the appropriate record for each author.

Open Funder Registry: Information about an article's funding sources is now submitted to Crossref to help you comply with current or future funding agency mandates. Crossref's Open Funder Registry (https://www.crossref.org/services/funder-registry/) is the definitive registry of funding agencies. Please ensure that your acknowledgments include all sources of funding for your article following any requirements of your funding sources. Where possible, please include grant and award ids. Please carefully check the following funder information we have already extracted from your article and ensure its accuracy and completeness: Horizon 2020, SFRH/BD/117448/2016

Other Items to Check

- Please note that the original manuscript has been converted to XML prior to the creation of the PDF proof, as described above. Please carefully check all key elements of the paper, particularly the equations and tabular data.

- Title: Please check; be mindful that the title may have been changed during the peer-review process.

- Author list: Please make sure all authors are presented, in the appropriate order, and that all names are spelled correctly.

- Please make sure you have inserted a byline footnote containing the email address for the corresponding author, if desired. Please note that this is not inserted automatically by this journal.

- Affiliations: Please check to be sure the institution names are spelled correctly and attributed to the appropriate author(s).

- Receipt date: Please confirm accuracy.

- Acknowledgments: Please be sure to appropriately acknowledge all funding sources.

- Hyphenation: Please note hyphens may have been inserted in word pairs that function as adjectives when they occur before a noun, as in "x-ray diffraction," "4-mm-long gas cell," and "R-matrix theory." However, hyphens are deleted from word pairs when they are not used as adjectives before nouns, as in "emission by x rays," "was 4 mm in length," and "the R matrix is tested."

  Note also that Physical Review follows U.S. English guidelines in that hyphens are not used after prefixes or before suffixes: superresolution, quasiequilibrium, nanoprecipitates, resonancelike, clockwise.

- Please check that your figures are accurate and sized properly. Make sure all labeling is sufficiently legible. Figure quality in this proof is representative of the quality to be used in the online journal. To achieve manageable file size for online delivery, some compression and downsampling of figures may have occurred. Fine details may have become somewhat fuzzy, especially in color figures. The print journal uses files of higher resolution and therefore details may be sharper in print. Figures to be published in color online will appear in color on these proofs if viewed on a color monitor or printed on a color printer.

- Please check to ensure that reference titles are given as appropriate.

- Overall, please proofread the entire *formatted* article very carefully. The redlined PDF should be used as a guide to see changes that were made during copyediting. However, note that some changes to math and/or layout may not be indicated.

Ways to Respond

- *Web:* If you accessed this proof online, follow the instructions on the web page to submit corrections.
- *Email:* Send corrections to prbproofs@aptaracorp.com
    Subject: **BS13965** proof corrections
- *Fax:* Return this proof with corrections to +1.703.791.1217. Write **Attention:** PRB Project Manager and the
    Article ID, **BS13965**, on the proof copy unless it is already printed on your proof printout.

Ca$_2$MnO$_4$ structural path: Following the negative thermal expansion at the local scale

Pedro Rocha-Rodrigues ⓘ,[1] Samuel S. M. Santos ⓘ,[1] Gonçalo N. P. Oliveira ⓘ,[1] Tiago Leal,[1] Ivan P. Miranda ⓘ,[2]

António M. dos Santos,[3] João G. Correia ⓘ,[4] Lucy V. C. Assali,[2] Helena M. Petrilli,[2]

João P. Araújo,[1] and Armandina M. L. Lopes ⓘ[1,*]

[1]*IFIMUP, Institute of Physics for Advanced Materials, Nanotechnology and Photonics, Departamento de Física e Astronomia da Faculdade de Ciências da Universidade do Porto, Rua do Campo Alegre, 687, 4169-007 Porto, Portugal*

[2]*Universidade de São Paulo, Instituto de Física, Rua do Matao, 1371, 05508-090, São Paulo, SP, Brazil*

[3]*Neutron Scattering Division, Oak Ridge National Laboratory, Oak Ridge, Tennessee 37831, USA*

[4]*C2TN, Centro de Ciências e Tecnologias Nucleares, Departamento de Engenharia e Ciências Nucleares, Instituto Superior Técnico, Universidade de Lisboa, Estrada Nacional 10, 2695-066 Bobadela LRS, Portugal*

The oxygen octahedral rotations in Ca$_2$MnO$_4$, the first member of the CaO(CaMnO$_3$)$_n$ Ruddlesden-Popper family, is probed through a set of complementary techniques, including temperature-dependent neutron and x-ray diffraction, combined with local probe studies and *ab initio* calculations. Here we demonstrate the enhancement of the uniaxial negative thermal expansion coefficient from -1.26 ± 0.25 to -21 ± 1.8 ppm/K at the second order $I4_1/acd$ to $I4/mmm$ structural phase transition, providing direct evidence for the corkscrew atomic mechanism. We establish, also, that the predicted $I4/mmm$ high symmetry is attained around 1050 K. At lower temperatures, within the 10–1000 K temperature range, our first-principles calculations and detailed analysis of the Ca local environment reveals that the reported *Aba*2 structural phase, coexisting with the $I4_1/acd$ one, cannot describe correctly this compound. On the other hand, our data allow for the coexistence of the locally identical $I4_1/acd$ and *Acam* structural phases.

I. INTRODUCTION

Materials are know to expand with increasing temperature, what is commonly referred to as positive thermal expansion (PTE). Nevertheless, a few materials exist which present negative thermal expansion (NTE), exhibiting a volume contraction when increasing temperature [1,2]. The technological relevance of tunable thermal expansion properties relies on obtaining the long-awaited zero thermal expansion, with potential to be used in high-precision optical and microelectronic devices [1,2]. Understanding the mechanism at the origin of these effects is a fundamental step towards fine tuning control [1–5]. Therefore, unraveling the detailed structural phase transition paths, when changing the temperature, is of key importance. Among the Ruddlesden-Popper (RP) systems, with general formula $A_{n+1}B_nO_{3n+1}$ (*A*: alkaline earth or lanthanide cation and *B*: transition metal), the Ca$_2$MnO$_4$ presents the highest uniaxial negative thermal expansion (NTE) of its series, exhibiting a contraction as high as 4.4 ppm/K along the stacking axis of its naturally layered perovskite structure [4,6]. The Ca$_2$MnO$_4$ structure consists of a stack of CaMnO$_3$ perovskite layers intercalated periodically with rocksaltlike CaO layers, as depicted in Fig. 1(a). The combination of a layered structure with the condensation of MnO$_6$ octahedral distortion modes, in the tetragonal $I4_1/acd$ phase, revealed to be extremely important to the enhancement of the

elastic anisotropy driving the NTE on this system, activated also by the presence of low energy phonon modes [4,7]. At the atomic scale, Abblit *et al.* proposed recently a corkscrew mechanism to clarify the anisotropic elastic compliance that operates specifically at perovskite/rocksaltlike layers interfaces. The atomic model that treats octahedra as rigid units, shows that the stiff nature of specific Ca-O bonds plays a crucial role in coupling the decrease of MnO$_6$ octahedra rotation to the lattice stacking-axis contraction [8]. Nevertheless, the Ca$_2$MnO$_4$ structural phases at distinct temperatures are still not clear. X-ray diffraction measurements performed by Takahashi and Kamegashira have shown that Ca$_2$MnO$_4$ exhibits the $I4_1/acd$ symmetry from 298 up to 977 K [9]. The $I4_1/acd$ phase is established by the ordering of one distortion mode, a rotation of the MnO$_6$ octahedra around the *c* axis, characterized by the P_4 irrep (irreducible representation) of the parent space group $I4/mmm$, schematically shown in Fig. 1(b). In the $I4_1/acd$ symmetry, equivalent MnO$_6$ octahedra undergo an antiphase rotation around the *c* axis. Anisotropic NTE, although not very common, has been reported in a number of similar RP compounds displaying analogous BO$_6$ rotation patterns [3,5,7,10,11]. Looking into the equivalent case of Sr$_2$RhO$_4$, it was observed that the transition from the $I4_1/acd$ to the $I4/mmm$ symmetry results in a change from the uniaxial NTE to a conventional PTE [10]. Ranjbar and Kennedy have shown that the related structural transition appears to be a continuous one, in which the amplitude of the MnO$_6$ octahedral rotations gradually decreases when going from the distorted $I4_1/acd$ phase to the undistorted $I4/mmm$ one [10].
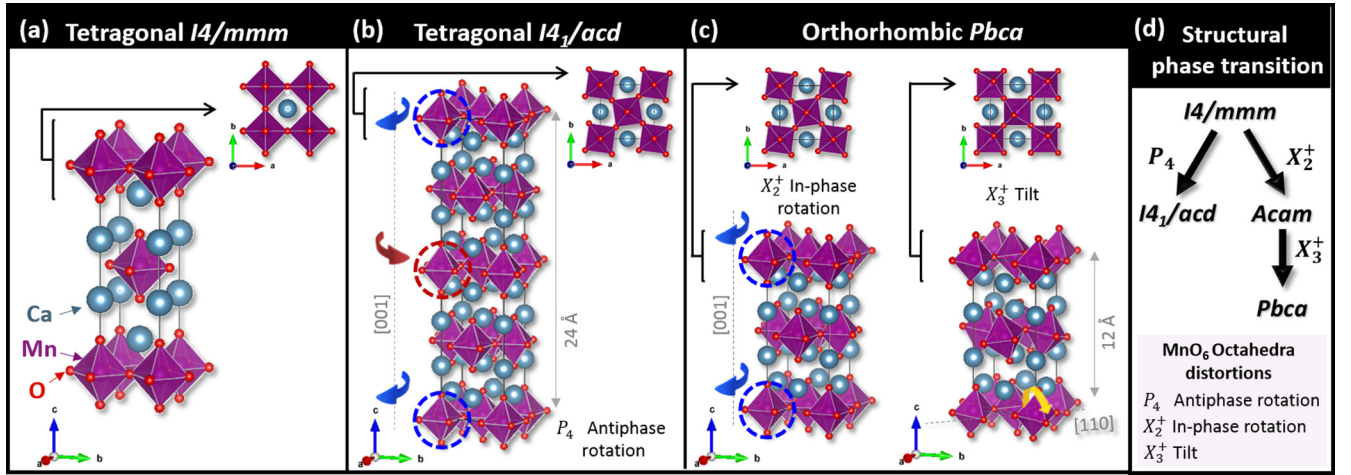
_____

*armandina.lopes@fc.up.pt

FIG. 1. Ca_2MnO_4 crystal structures and related group-subgroup tree. (a) Representation of the Ca_2MnO_4 structure in the parent space group $I4/mmm$, in which blue and red spheres represent, respectively, the Ca and O ions and the Mn ions are represented at the center of each illustrated octahedron. Illustration of the MnO_6 octahedra distortion modes present in the distinct structural phases: (b) $I4_1/acd$ and (c) $Pbca$. Red/blue circles highlight equivalent MnO_6 octahedra belonging to neighbor perovskite layers, and the colored arrows the orientation of the respective octahedral rotations. (d) Space group symmetry pathway among the $I4/mmm$, $I4_1/acd$, $Acam$, and $Pbca$ structural phases.

Furthermore, Takahashi and Kamegashira have predicted that the structural transition from the $I4_1/acd$ to the high symmetric $I4/mmm$ in Ca_2MnO_4 would occur at ≈ 1500 K [9].

Neutron diffraction measurements carried out for Ca_2MnO_4 at lower temperature ranges (<500 K), have shown that the experimental results could be fitted within the $I4_1/acd$ space group [4,7,12]. However, Autret *et al.* have shown that Ca_2MnO_4 presents a relative lower structural coherence length along the $I4_1/acd$ c axis. From transmission electron microscopy measurements performed at room temperature, they have proposed a coexistence of two structural phases, with apparently random stacking along the c axis of the tetragonal $I4_1/acd$ and the orthorhombic $Aba2$ phases in Ca_2MnO_4 [12]. The authors have then proposed that in the $Aba2$ structural phase the MnO_6 octahedra rotate also around the c axis, but unlike the $I4_1/acd$ phase, the MnO_6 octahedra, in equivalent perovskite slabs, undergo an in-phase rotation. This results in a lower structural periodicity along the c axis, ≈ 12 Å, when compared to ≈ 24 Å of the $I4_1/acd$ phase; the appearance of a secondary phase (with in-phase rotations) leads to the coherence length reduction along the stacking axis, the average length scale of coherent out-of-phase rotations of the MnO_6 octahedra [12]. It was also mentioned that the $Aba2$ structural phase may present an extra MnO_6 octahedral tilting mode around the c axis. However, no structural data regarding the amplitude of any of these distortions have been provided [12]. Recently, DFT calculations considering the analogous Ca_2GeO_4 compound, have shown that the corresponding ground-state structure should present an orthorhombic $Pbca$ symmetry, whose lattice distortions are identical to the ones mentioned for the $Aba2$ space group [6]. Namely, an in-phase rotation around the c axis (irrep X_2^+) and an extra tilting mode of the MnO_6 octahedra around the [110] direction (irrep X_3^+), as shown in Fig. 1(c) [6].

Nuclear hyperfine radioactive techniques, particularly the time differential perturbed angular correlations γ-γ technique

(PAC), provide excellent resources on studies aimed to disentangle local structural changes at the nanoscopic scale. The local character of the PAC technique, and its temperature-independent signal quality, makes this nuclear spectroscopy technique particularly useful in studying structural phase transitions, which are not easily identified or characterized by diffraction experiments [13,14]. By using ^{111m}Cd as the probe isotope we have measured, in the 10–1200 K temperature range, the distributions of the electric field gradient (EFG) at the nucleus at the Ca site. The EFG characterizing the surrounding charge density that interacts with a probe nucleus, is a second order symmetric and traceless tensor with principal axis components V_{xx}, V_{yy}, and V_{zz} such that $|V_{zz}| \geqslant |V_{yy}| \geqslant |V_{xx}|$. V_{zz} and the asymmetry parameter $\eta = (V_{xx} - V_{yy})/V_{zz}$ fully describe the observable hyperfine interaction [15].

Herein we show that by combining the EFG experimental measurements with *ab initio* calculations and neutron diffraction technique, the MnO_6 octahedra that surround the ^{111m}Cd probe, ultimately underlying the Ca_2MnO_4 structural phase transitions and functional properties, can be detailed characterized. Additionally, we show that while the neutron diffraction measurements were not able to distinguish properly between the $I4_1/acd$ and $I4/mmm$ symmetries at high temperatures, the PAC results, which provide local symmetry information, were determinant to clearly identify the critical temperature of the transition from the $I4_1/acd$ phase to the $I4/mmm$ one. We correlate this transition, and its second order nature, with the enhancement of the uniaxial NTE that we observed in Ca_2MnO_4 by x-ray and neutron diffraction, close to the critical temperature, providing direct evidence for the corkscrew atomic mechanism that was theoretically proposed by Ablitt *et al.* [6,8]. At low temperatures, following the reported low structural coherence length along the c axis at room temperature, we discuss the possible coexistence of the locally identical $I4_1/acd$ and $Acam$ structural phases.

II. METHODS

A. Experimental details

Polycrystalline samples of Ca$_2$MnO$_4$ were prepared by solid state reaction. Stoichiometric quantities of CaCO$_3$ (99.0%, Sigma-Aldrich) and MnO$_2$ (99.99%, Sigma-Aldrich) were mixed, pressed into pellets, followed by a 3 h heat treatment at 1123 K. Four additional grinding and heating cycles were performed at 1473 K in air atmosphere (12 h). A single phase sample was confirmed by x-ray powder diffraction. *In situ* high temperature x-ray powder diffraction was performed in a PANalytical X'Pert Pro MPD, equipped with a XRK-900 stage, data were collected in a continuous mode at constant temperature steps with a 5 min stabilization temperature, and *in situ* high temperature neutron diffraction was performed using a POWGEN instrument at the Spallation Neutron Source (SNS), data were collected at 298, 673, 973, and 1223 K. All of the high temperature diffraction measurements were performed at a vacuum level of $\approx 2 \times 10^{-5}$ Torr. The collected data was analyzed with the FULLPROF software package [16] and the structures were drawn using VESTA software [17].

The γ-γ PAC measurements [15] were made on pellet samples that were implanted with radioactive ^{111m}Cd ions that, owing to their similar ionic radius and charge, easily substitute Ca^{2+} in the Ca$_2$MnO$_4$ system [13,18]. As shown by *ab initio* calculations for the homologous Ca$_3$Mn$_2$O$_7$ compound, this ionic substitution does not produce significant distortions into the original crystal lattice [13]. The implantation was performed at ISOLDE-CERN with 30 keV energy beam, and low dose below 1 ppm of the Ca/Mn atomic concentrations. Subsequently, the samples were air annealed at 1123 K for 20 min to remove residual implantation point defects. Due to the short lifetime of the parent ^{111m}Cd probe, every temperature point required a new implantation-annealing-measurement $\sim$4 h cycling. Crystalline quality of the sample post implantation-annealing process was later confirmed by x-ray diffraction.

The ^{111m}Cd probes decay to ^{111}Cd through an intermediate state by the emission of two consecutive γ rays. The half-life for the ^{111m}Cd isomeric state is 48 min, while for the intermediate state is 84 ns. The angular correlation between the two γ rays can be perturbed by the EFG and existent magnetic hyperfine fields (MHF). Both the EFG and MHF couple to the nuclear electric quadrupole Q and the magnetic dipole ($\vec{\mu}$) moments of the ^{111m}Cd intermediate nuclear state. The Hamiltonian for such static interactions, in the proper reference frame of the EFG tensor V_{ij}, with $|V_{zz}| \geqslant |V_{yy}| \geqslant |V_{xx}|$, reads

$$\mathcal{H} = \frac{\hbar \omega_0}{6e} \left[3I_z^2 - I(I+1) + \frac{1}{2}\eta(I_+^2 + I_-^2) \right] + \vec{\mu} \cdot \vec{B}_{\text{hf}}, \quad (1)$$

where $\omega_0 = 3eQV_{zz}/[2I(2I-1)\hbar]$ is the fundamental precession frequency, I represents the nuclear spin of the probe intermediate state, $\eta = (V_{xx} - V_{yy})/V_{zz}$ is the EFG asymmetry parameter, and $\vec{B}_{\text{hf}}$ is the magnetic hyperfine field [15,19–22]. Below Ca$_2$MnO$_4$ antiferromagnetic transition (110 K) [12], in the presence of the two fields, we apply combined interaction theory to obtain the MHF and EFG parameters, above T_N, pure static electric quadrupole interactions were considered. In the case of a static electric quadrupole interaction, the time dependent perturbation factor on the observable gamma-ray angular anisotropy of the decay cascade $G_{kk}(t)$ can be described as a sum of periodic terms, where t is the time spent by the nucleus in the ^{111m}Cd intermediate probing state. In the presence of EFG distributions the periodic terms are attenuated, here represented by a Lorentzian attenuation function characterized by its relative width δ:

$$G_{kk}(t) = S_{k0} + \sum_n S_{kn} \cos(\omega_n t) e^{-\delta \omega_n t}. \quad (2)$$

The frequencies represented by ω_n are those of the transition between the hyperfine levels created when a nuclear state is split by the hyperfine interaction (in the case of ^{111m}Cd the intermediate level is characterized by nuclear spin momentum of $I = 5/2$). The quadrupole interaction splits this level into three sublevels and thus in the respective Fourier transform (FT) we observe a triplet of frequencies (ω_1, ω_2, ω_3, where $\omega_3 = \omega_1 + \omega_2$) for each nonvanishing EFG distribution present in the system. For a static interaction the anisotropy function obtained experimentally can be written as $R(t) = \sum A_{kk} G_{kk}(t)$, where A_{kk} are the angular correlation coefficients of the nuclear decay cascade. Further experimental details can be seen in Refs. [19,23].

B. First-principles calculations

From *ab initio* calculations we have obtained the hyperfine parameters for the Ca site in the Ca$_2$MnO$_4$ system. These properties were obtained for the three distinct phases that Ca$_2$MnO$_4$ can exhibit: $I4_1/acd$, *Acam*, and $I4/mmm$. We used the all-electron full-potential linearized augmented plane wave (FP-LAPW) method [24], implemented in the WIEN2K computational package [25]. The calculations were performed within the framework of the density functional theory (DFT) [26,27], using the Perdew-Burke-Ernzerhof generalized gradient approximation (PBE-GGA) for the exchange-correlation potential [28]. The cut-off energy was set to $RK_{\max} = 7.0$, which defines the total number of plane waves to describe the electronic wave functions in the interstitial region, where R is the sphere radius for the smallest atomic region. The self-consistency was achieved when the difference in total energy between two consecutive iterations was less than 10^{-4} Ry. Brillouin zones for the electronic states were sampled by a Γ-centered $12 \times 12 \times 12$ **k**-point mesh, generated according to the Monkhorst-Pack scheme [29]. Tolerance for differences in intracell atomic positions were set to the fourth decimal place. In order to study the thermal evolution of the hyperfine properties, we set forth two procedures. First, the simulations were performed using experimental atomic positions of the $I4_1/acd$ phase within the 298–977 K temperature range [9]. Then, new simulations were carried out using new structures that were generated for distinct amplitudes of the MnO$_6$ octahedral rotation (irrep P_4), through the ISODISTORT software [30,31], following the transition path from the $I4_1/acd$ phase to the $I4/mmm$ one. In both phases, the DFT electronic self-consistent cycles were conducted with no relaxation of the atomic positions or the lattice parameters. Furthermore, simulations were also performed to obtain the ground state theoretical structural parameters of the $I4_1/acd$

and *Acam* phases of the Ca_2MnO_4 compound. For these specific cases, the calculations were based on the plane-wave, pseudopotential DFT method as implemented in the QUANTUM ESPRESSO code suite [32,33]. The properties were obtained using the projector augmented wave (PAW) formalism [34] together with the PBE-GGA exchange-correlation functional. Plane-wave cutoffs of 115 and 500 Ry for the wave function and density, respectively, were adopted. The Brillouin zones for the electronic states were sampled by a Γ-centered $8 \times 4 \times 8$ and $8 \times 8 \times 4$ Monkhorst-Pack **k**-point mesh for the *Acam* and the $I4_1/acd$ phases, respectively. In order to maintain the consistency with other EFG results presented in this work, the V_{zz} and η values for these ground states were obtained with the WIEN2K code, using the optimized structures obtained with the QUANTUM ESPRESSO code.

It is worth mentioning that the *A*-, *C*-, and *G*-type antiferromagnetic (AFM) ordering as well as the ferromagnetic (FM) one were simulated and the ground state of the *Acam* and the $I4_1/acd$ phases of the Ca_2MnO_4 presented the *G*-type AFM alignment with similar hyperfine, energetic, and structural properties. The spin magnetic moment at Mn sites were ± 2.26 μ_B/atom for both phases, as well the direct (Γ-Γ) band gap was of ≈ 0.8 eV. Calculations using the GGA+U approach with the Hubbard correction $U = 4.5$ on the Mn $3d$ states [35] were also performed and, as expected, both the band gap and the Mn spin magnetic moments increased. The band gap acquired the values of ≈ 1.0 and ≈ 0.9 eV for the $I4_1/acd$ and *Acam* structures, respectively, in good agreement with theoretical [36] and experimental [37] values. The magnetic moment value increased to ± 2.61 μ_B/atom, for both phases, in very good agreement to the one obtained by Matar *et al.* [36]. The hyperfine quantities as well the energetic and structural ones remained unchanged.

III. RESULTS/DISCUSSION

The experimental results obtained by PAC, x-ray, and neutron diffraction are presented in Fig. 2. The experimental $R(t)$ anisotropy function, the PAC observable, together with the FT of the fits are presented in Fig. 2(a). The fits to the $R(t)$ experimental data were performed considering electric quadrupole interactions and static regular EFG distributions, assumed to be Lorentzian-like. The global fits to the $R(t)$ functions are shown by the thick continuous black lines in the spectra. In the highest temperature region, identified in Fig. 2(a) as the F2 environment, a single axially symmetric EFG, a signature for a highly symmetric local environment, is evidenced by the equidistant frequency triplet in the FT. At lower temperatures, a second frequency doublet characteristic of an axially asymmetric EFG is present, labeled in Fig. 2(a) as the F1 environments. As previously mentioned, for the nuclear spin 5/2 of the ^{111m}Cd PAC probe, a triplet of observable frequencies and amplitudes is expected, fully characterizing each EFG. Ongoing from axially symmetric EFG ($\eta = 0$) to the lowest axial symmetry ($\eta = 1$), two of the three frequencies converge, leading to two observable ones. The $R(t)$ function is then a linear combination of perturbation functions characteristic of each different probe environment, different EFGs, weighted by the corresponding fraction of

probe atoms interacting with it. The fitting parameters obtained for the distinct measuring temperatures, such as the EFG principal component V_{zz}, and the axial asymmetry parameter η, are presented in Figs. 3(a) and 3(b), respectively. For the experimental data acquired below 100 K, we applied combined interaction theory to obtain the MHF parameters as well from the fits to $R(t)$. Below Ca_2MnO_4 antiferromagnetic transition temperature [12], an increasing local average magnetic hyperfine field at the Ca site ($|B_{hf}|$) is measured upon decreasing temperature, presenting at 10 K a magnitude of the order of $\approx 0.99 \pm 0.02$ T (Fig. S1) [38].

The temperature dependent neutron and x-ray diffraction profiles for Ca_2MnO_4 are shown in Figs. 2(b) and 2(c), respectively. At room temperature, the neutron diffraction data, unlike the x-ray diffraction measurements, are able to distinguish easily the Bragg peaks expected for the $I4_1/acd$ structural phase [indexed in Fig. 2(b) by the blue stars]. Note that, despite the higher space group number of the low temperature phase, its volume is four times larger ($\sqrt{2}$ in a/b and a factor of 2 along c), resulting in extra allowed reflections when compared to the high temperature $I4/mmm$ phase. The lower sensitivity of the x-ray diffraction to distinguish between the $I4/mmm$ and $I4_1/acd$ structures is expected since the transition from $I4/mmm$ to $I4_1/acd$ phase is related to the displacement of the MnO_6 equatorial oxygen atoms. A relative intensity decreasing of the $I4_1/acd$ exclusive peaks is observed upon heating, being the remaining $h, k, l = (2, 1, 1)$ Bragg contribution barely visible at 973 K. By comparison with the PAC results, a high local axial asymmetry at the Ca site, expected for the $I4_1/acd$ phase, is still observed in Fig. 2(a) at 988 K. Although not used for space group indexation, the x-ray diffraction measurements provide an easy way to study the thermal evolution of the Ca_2MnO_4 lattice parameters. Up to approximately 1050 K, the x-ray and neutron diffraction patterns were refined within the $I4_1/acd$ symmetry; for higher temperatures the results could be refined within the $I4/mmm$ symmetry. The respective structural parameters are presented in Fig. 3(c).

A. Ca_2MnO_4 high temperature structural transition and thermal expansion properties

In Fig. 3(a) it can be observed that, globally, the $|V_{zz}|$ thermal dependency follows the most common trend observed in EFG measurements, i.e., a magnitude decrease with increasing temperature [39,40]. Kushida has shown that if one considers harmonic vibrations around the atom's equilibrium positions, such as rotations modes of frequency f, at sufficiently high temperatures ($k_B T \gg f$) the $|V_{zz}|$ should decrease linearly with increasing temperature [39,40]. The fit to the experimental data regarding the F1 data (pink line), presented in Fig. 3(a), was performed considering a single phonon contribution model, from which we have obtained the value $f = 6.60 \pm 0.85$ THz, close to the estimated lowest energy vibration frequency of ≈ 5.43 THz that is supposed to drive Ca_2MnO_4 uniaxial NTE [7]. The contribution of higher frequency modes to the temperature dependence of $|V_{zz}|$ is known to be much less important than the contribution from low frequency modes [39,40]. Within the 1000–1200 K temperature range, a small shift in the thermal dependency of $|V_{zz}|$ is
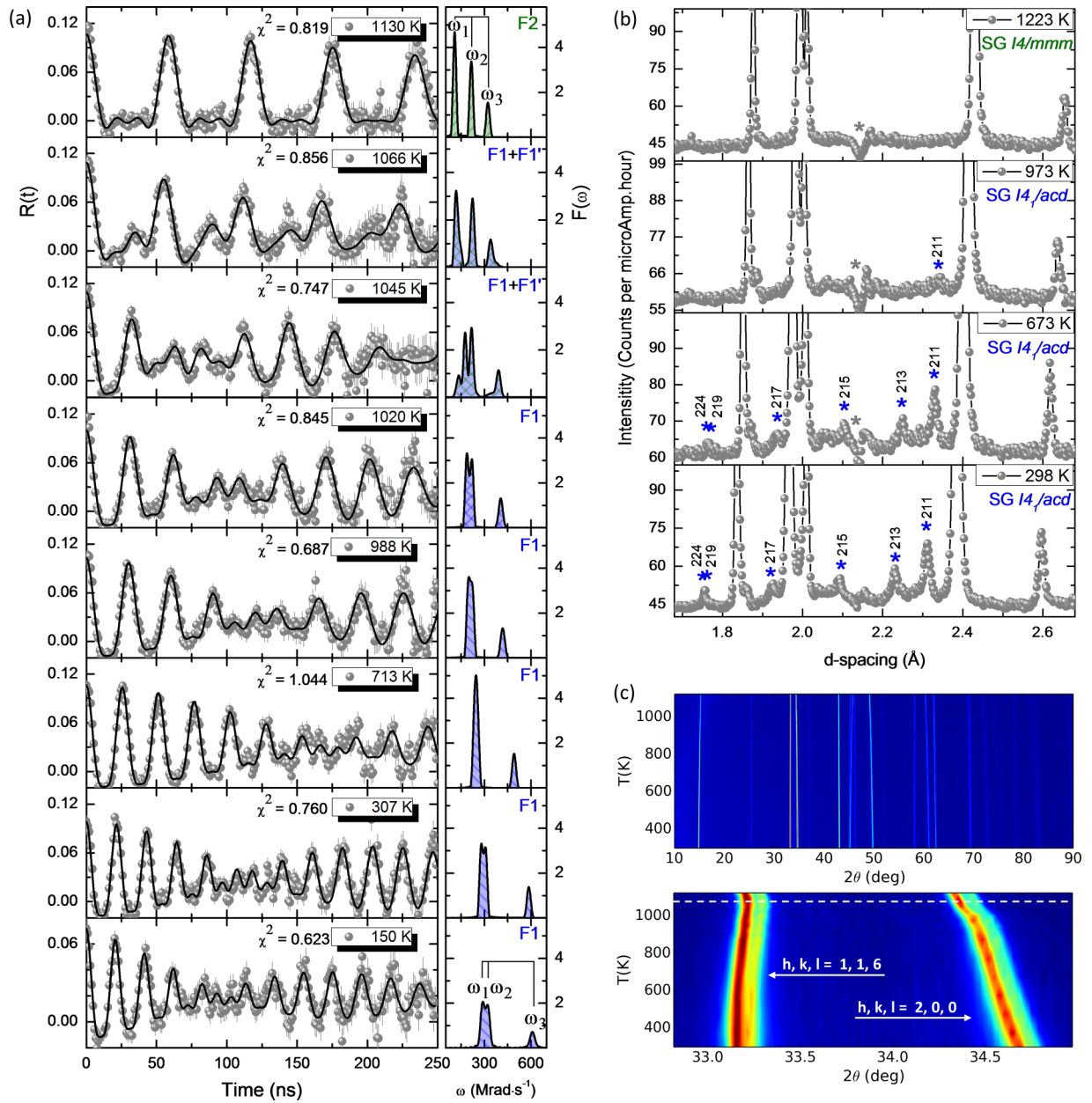
FIG. 2. Ca$_2$MnO$_4$ experimental results. (a) Representative $R(t)$ functions, corresponding fits, and respective FT taken at different temperatures for the ^{111m}Cd parent probes. (b) Neutron diffraction profiles at 298, 673, 973, and 1223 K, highlighting the reflections sensitive to the octahedra structure and rotations, exclusive of the $I4_1/acd$ space group (indexed by the blue stars). The feature in the spectra, in the regions marked by the gray stars, arises from the Bragg scattering of the vanadium dataset for the incident spectra normalization procedure. (c) 2D contour plot of the x-ray diffraction patterns, where each one of them has been normalized to the highest peak, and thermal displacement of the Bragg peaks defined as $h, k, l = (1, 1, 6)$ and $h, k, l = (2, 0, 0)$. The white dashed line separates the temperature range into the uniaxial NTE and PTE regions.

observed. However, by inspecting Fig. 3(b), a clear transition from a local environment of low axial symmetry $\eta \approx 0.8$ to another of high axial symmetry $\eta \approx 0$ is detected. This is clearly perceived in the frequency domain of the experimental PAC data, in Fig. 2(a), in the transition, with increasing temperature, from the frequency doublet (blue shaded) to the frequency triplet (green shaded) of lower quadrupole frequency. We interpret these results as a direct evidence for the $I4_1/acd$ to the $I4/mmm$ structural phase transition. A high axial symmetry is expected at the Ca site for the $I4/mmm$

phase, as the symmetry group of this Wyckoff position contains a rotational fourfold axis parallel to the unit cell c axis, which can be verified in Fig. 1(a) from the c axis perspective representation of the Ca$_2$MnO$_4$ structure.

With the support of DFT calculations, the evolution of V_{zz} and η values for the Ca nuclei was studied as a function of the amplitude of MnO$_6$ octahedral rotation (irrep P_4), as shown in Fig. 4. The white squares series was calculated using experimental atomic positions from the literature [9]. For the blue diamond series, the Ca$_2$MnO$_4$ lattice constants and extra
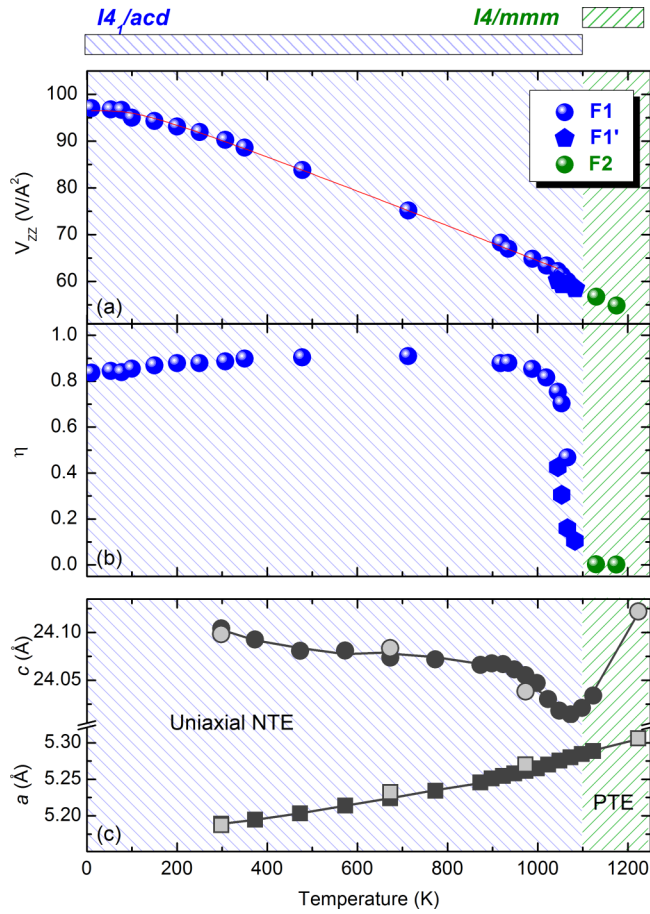
FIG. 3. Experimental electric field gradient and lattice parameters for the Ca_2MnO_4 sample. (a) EFG principal component magnitude $|V_{zz}|$ (pink continuous line correspond to the fit of F1 experimental $|V_{zz}|$ obtained using Kushida's model for a single phonon contribution [39,40]); (b) asymmetry parameter η; and (c) temperature evolution of the Ca_2MnO_4 lattice parameters a ($=b$) and c. The dark and light gray markers represent the data collected by x-ray and neutron diffraction techniques, respectively. For the $I4/mmm$ phase, $\sqrt{2}a$ and $2c$ values are plotted. The gray lines are guides for the eyes.
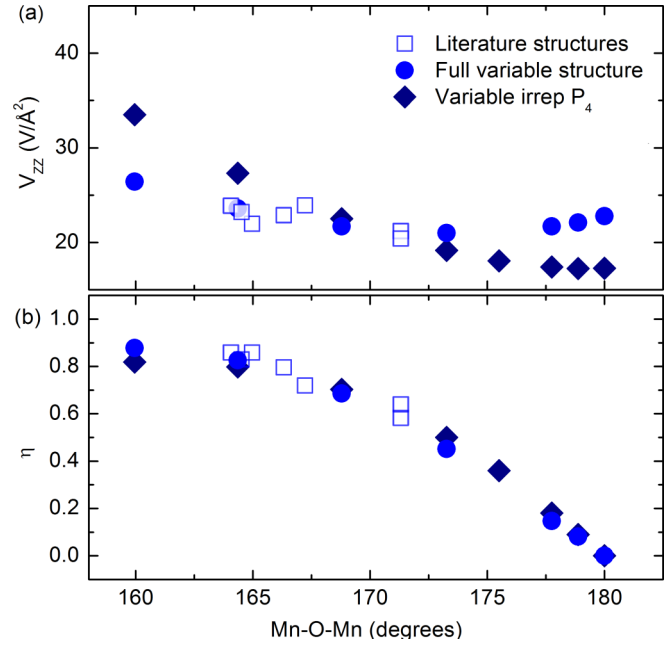

FIG. 4. Theoretical EFG parameters at Ca site as a function of increasing Mn-O-Mn bond angle. White squares were calculated by using the x-ray diffraction structural parameters of Takahashi and Kamegashira [9]. The blue circles represent the data acquired by simulating the Ca_2MnO_4 with the structural parameters obtained by a linear extrapolation of the lattice distortions evolution as a function of the P_4 MnO_6 amplitude of rotation. The blue diamonds are the results obtained by changing solely the amplitude of the P_4 MnO_6 rotation, maintaining the other structural parameters unchanged, same as the ones reported for the structure measured at 977 K [9]. (a) V_{zz} and (b) asymmetry parameter η.

lattice distortion modes were maintained fixed and equal to the experimental values as measured at 977 K by Takahashi and Kamegashira [9]. Solely the amplitude of MnO_6 octahedra rotation (irrep P_4) was changed. For the blue circle series, the lattice parameters and extra distortion modes, such the Ca and apical O displacement modes along c axis, were calculated by linear extrapolation (interpolation) from the Takahashi and Kamegashira crystallographic data [9]. In Fig. 4(b) it can be noted that, regardless the exact z coordinates for the Ca site, for both simulated cases (blue circles and blue diamonds), the η parameter follows the same trend, decreasing from $\eta = 0.8$ to $\eta = 0$ with the increase of the Mn-O-Mn angle from 158° to 180° (undistorted $I4/mmm$ lattice). We observe that the sensitivity of the asymmetry parameter η to detect changes in the octahedra rotation should decrease in the range of angle values below $\approx 168°$. In Fig. 2(b) we can observe that the experimental asymmetry parameter remains relatively high and almost constant up to 900 K. This trend is then followed by a sharp decrease to $\eta = 0$ at ≈ 1050 K. Considering our

simulations, this behavior suggests that in the 900–1100 K temperature range the Mn-O-Mn angle sharply increases in the range from $\approx 170°$ to 180°. From the neutron diffraction results taken at 973 K, Fig. 2(b), we have estimated a Mn-O-Mn bond angle of 172.49(9)°. This apparent discrepancy from the local probe results might suggest that here the Mn-O-Mn bond angle might be overestimated by the crystallographic approach, based on a long range average model. Throughout the MnO_6 octahedra rotation, the principal axis of the EFG tensor associated with the V_{zz} component remains parallel to the c axis of the $I4_1/acd$ unit cell. When comparing the order of magnitude of $|V_{zz}|$ for the Ca nuclei with the experimental results shown in Fig. 3(a), one of the main differences is related to the fact that in PAC experiments the polarization of the probe's internal orbitals amplifies the EFG, compared to the Ca ones, by the so-called Sternheimer antishielding effect [15]. The ratio of this amplification, comparing Ca : Cd inner electron orbitals, is known from the literature to be around of $\approx 1 : 2$ [13]. Furthermore, it is worth to remember that the theoretical results were obtained either from experimental atomic positions of the Ca_2MnO_4 or from structures simulated by using the ISODISTORT software [30,31] but, in any case the simulations were performed considering the effect of Cd as an impurity.

Regarding the nature of the $I4_1/acd$ to the $I4/mmm$ structural transition, a smooth variation of the Ca_2MnO_4 lattice

parameters a and c can be observed in Fig. 3(c), as expected for a second order structural transition. In a concomitantly but independent way, the EFG data shows a continuous change from a low axial symmetry ($\eta = 0.9$) to a high axial symmetry environment ($\eta = 0$), as a function of temperature. As reported for the Sr$_2$RhO$_4$, our PAC experimental results indicate that the thermal rate of the MnO$_6$ rotation variation (irrep P_4) increases sharply near the critical temperature. Complementary, the local scale EFG data shows that well before the $I4/mmm$ high-symmetry phase is achieved, the experimental $R(t)$ functions measured at ≈1050 K can only be properly fitted by considering two local environments distributions with distinct EFG η parameters ($\eta_1 \approx 0.8$–0.4, $\eta_2 \approx 0.4$–0.1). This reveals the second order nature of the $I4_1/acd$ to the $I4/mmm$ structural transition, thought being of the displacive type, where the coexistence of the local environments with distinct η parameters could be linked, within the $I4_1/acd$ symmetry, with distinct amplitudes of the MnO$_6$ octahedral rotation (irrep P_4) [Fig. 4(b)]. It is known that even in continuous phase transitions driven by soft phonon modes, the structural transformations do not occur at once. The critical temperature of the $I4_1/acd$ to $I4/mmm$ structural transition may have a distribution at the local scale arising from, e.g., the presence of defects or mosaic structure, that prevent lattice modes running evenly through the whole crystal [41]. Furthermore, following Landau phase transition theory, at the critical temperature the structure of the Ca2MnO$_4$ compound may fluctuate between the $I4_1/acd$ and $I4/mmm$ symmetries with no energy cost [41]. Therefore, close to the phase transition critical temperature of ≈1050 K, distinct fractions of the ^{111m}Cd nucleus ensemble (F1 and F1′) statistical probe intermediate degrees of the rotation of the MnO$_6$ octahedra. We believe that this signature is averaged out when studying Ca$_2$MnO$_4$, or other analog compounds, with long range based characterization techniques.

Although one can tune the magnitude of uniaxial NTE upon A/B-site cation substitution, even for a certain chemical composition, a thermal dependency of the anisotropic NTE is generally observed, being especially preeminent near the critical transition temperatures [5,10]. In Ca$_2$Mn$_{1.4}$Ti$_{0.6}$O$_4$ and Sr$_2$RhO$_4$ compounds, for instance, close to the onset of the $I4/mmm$ symmetry, enhancement of the uniaxial NTE coefficients were observed from around -2 to -12 ppm/K, and from around -9 to -42 ppm/K, respectively [5,10]. In our results we observe a similar enhancement, from -1.26 ± 0.25 to -21 ± 1.8 ppm/K, that follows the decrease of the EFG axially asymmetry parameter η, i.e., the increase of the Mn-O-Mn bond angle. The lattice expansion coefficients (α) were extracted from Fig. 3(c) by applying the standard $\alpha = (1/c_0)\Delta c/\Delta T$ expression, in which $\Delta c/\Delta T$ was approximated from the linear fitting slope of the experimental lattice parameters within the respective temperature windows: 673–923 K and 973–1052 K. This enhancement of the uniaxial NTE coefficient agrees with the theoretical computational results of Ablitt *et al.* on the atomic structure for the structural equivalent (4.3 GPa biaxially stressed) Ca$_2$GeO$_4$ compound where, following the corkscrew mechanism within the $I4_1/acd$ symmetry, the contraction of the c axis is expected for decreasing rotation of the MnO$_6$ octahedra; i.e., a sudden decrease of the MnO$_6$ octahedra rotation should result in a sudden increase of lattice contraction along the c axis. On the other hand, as the compressive strain along c axis is coupled to the in-plane tensile strain, this also reflects in an increase of the thermal expansion for the $a(/b)$ lattice parameter, namely from 23.9 ± 1.4 to 35.9 ± 2.4 ppm/K for the mentioned temperature windows [5]. The former value agrees with the thermal tendency in Ca$_2$MnO$_4$, also observed by Takahashi and Kamegashira on the temperature range 548–977 K, around 20 ppm/K [9].

In our experiment, it can be observed that the thermal switch from uniaxial NTE to PTE occurs once the $I4/mmm$ phase is reached. In the work of Ranjbar and Kennedy, the switch to the $I4/mmm$ symmetry of the Sr$_2$RhO$_4$ compound is reported to occur within the 850–950 K temperature range, in which an intermediate uniaxial near zero thermal expansion is observed [10]. Meanwhile, in the Yoshida *et al.* work, the uniaxial NTE persists even in the $I4/mmm$ structure of the Sr$_3$Sn$_2$O$_7$ compound [11]. In spite of that, doubts arise, in the latter case, as to whether the Sr$_3$Sn$_2$O$_7$ structural phase is correctly indexed since, by comparing our neutron diffraction results with the experimental PAC ones (Fig. 2), it can be noticed that the $I4_1/acd$ phase exclusive Bragg peaks are difficult to detect at temperatures below the onset of the $I4_1/acd$ to $I4/mmm$ transition [Fig. 2(b)], while for the PAC results a high local axial asymmetry at the Ca site is still observed [Fig. 2(a)].

B. On the coexistence of the $I4_1/acd$ and $Aba2$ structural phases

In contrast with the transmission electron microscopy results reported by Autret *et al.* [12], our local probe results only attest to one, well defined, local environment at room temperature conditions [see experimental data at 307 K in Fig. 2(a)]. However, as reported by Autret *et al.*, in the process of fitting the neutron diffraction experimental pattern we observe an anomalous relative broader width of the reflections that distinguish $I4_1/acd$ from the $I4/mmm$ structure, specified by the $l = 2n + 3$ rule, an indication of the previously reported low structural coherence length along the Ca$_2$MnO$_4$ stacking axis (Fig. S2, Table S1) [12,38]. For the Ca$_2$MnO$_4$ compound that hosts a structural coexistence of the $I4_1/acd$ and $Aba2$ phases, it should be expected to measure two distinct EFG distributions. Considering that the extra tilting mode of the $Aba2$ phase, comparing to the $I4_1/acd$ phase, affects directly the nearest-neighbor oxygen atoms of the probe, one should expect to measure a second EFG distribution of smaller $|V_{zz}|$ [13]. Therefore, in order to explain the low structural coherence length measured along the c axis [12] we propose that the extra tilting of the $Aba2$ phase in fact does not condense, and thus the extra structural phase could be described within the higher symmetric $Acam$ group. The $Acam$ exhibits only the in-phase rotation around the c axis between equivalent MnO$_6$ octahedra, described by the distortion mode of X_2^+ symmetry as depicted in Fig. 1(c). Both $I4_1/acd$ and $Acam$ structural phases are identical from a local perspective yet exhibiting different periodicities along the c axis, respectively, of ≈24 and ≈12 Å [12].

Recently, DFT calculations for the analog Ca$_2$GeO$_4$ compound have shown that the lattice parameters, relaxed cell energies, and octahedral rotation angles are identical for

TABLE I. First-principles structural and hyperfine properties of the Ca_2MnO_4 optimized structures for both $I4_1/acd$ and *Acam* phases in the *G*-type antiferromagnetic alignment ground state.

	$I4_1/acd$ (No. 142)	*Acam* (No. 64)
a (Å)	5.189	5.190
b (Å)	5.189	5.190
c (Å)	24.446	12.220
$\angle$ Mn-O-Mn (deg)	158.7	158.8
$\|\Delta E\|$ (meV)	0	1.2
$\|V_{zz}\|$ (V/Å^2)	27.6	28.0
Main direction	c axis	c axis
η	1.0	1.0

the *Acam* and $I4_1/acd$ phases [6]. We have also performed structural relaxation of the Ca_2MnO_4 for both $I4_1/acd$ and *Acam* symmetries, and observed as well that the structural parameters and relaxed cell energies are identical, as can be verified in Table I, which would enable the coexistence of both phases. Moreover, assuming that the $I4_1/acd$ and *Acam* structural phases have the same Mn-O-Mn distortion angles, we observe that, from the point of view of the ^{111m}Cd probe, both structures are identical in a region with a radius up to ≈ 8 Å, as illustrated in Fig. 5. Here the probe nearest structural difference arises from the relative orientation of the rotation of the MnO_6 equatorial oxygen atoms. Consequently, the theoretical results show that the $\|V_{zz}\|$ and η values should be indistinguishable for these two structural phases when measured using the PAC technique.

IV. CONCLUSIONS

Summarizing, our combined experimental and *ab initio* studies allowed us to probe accurately the MnO_6 octahedral rotations underlying the material's structural transitions and its NTE behavior properties. Our studies confirm that the phase that stabilizes at the highest temperatures has the $I4/mmm$ symmetry, establishing also the critical temperature for this second order phase transition to be around 1050 K, at much lower temperature than previously predicted [9]. We provide direct evidence for the corkscrew atomic mechanism governing the enhancement of the uniaxial NTE close to the critical temperature [5,6,8]. The transition from uniaxial NTE to typical PTE occurs concomitant with the structural transition. Moreover, in the 10–1000 K temperature range we only found evidence for a single local environment. Herein, in order to explain the lower coherence length observed along the c axis in previous transmission electron microscopy measurements, we propose that the reported $Aba2$ structural phase of the Ca_2MnO_4 should be described instead in the higher symmetry *Acam* phase.
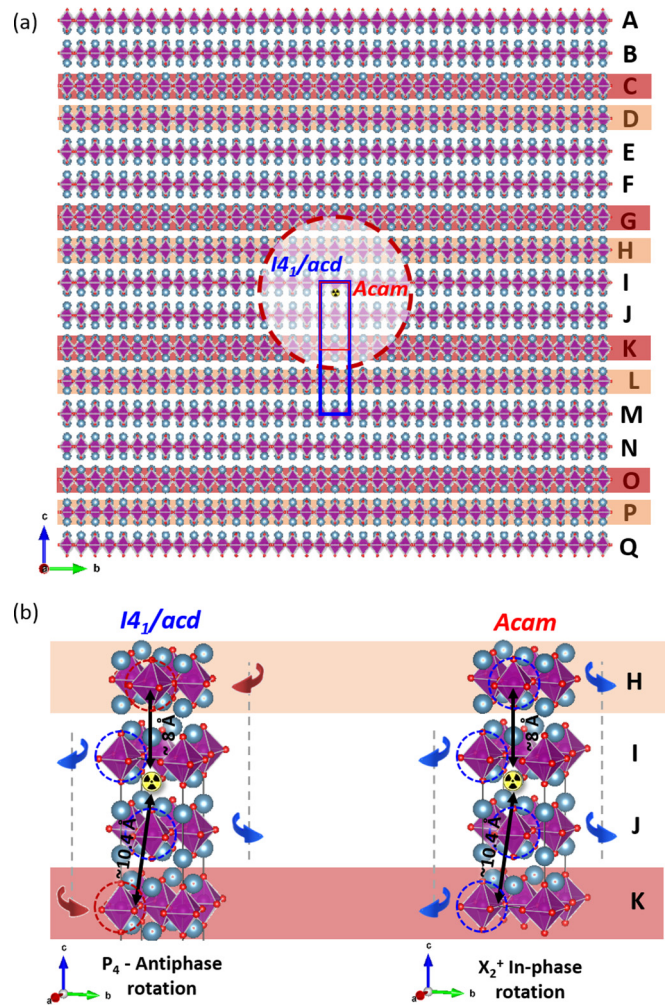
ACKNOWLEDGMENTS

FIG. 5. Comparison between the $I4_1/acd$ and *Acam* structural phases of the Ca_2MnO_4 compound from the ^{111}Cd local perspective: (a) perovskite slabs (orangish shading) in which the equatorial oxygen ions of the MnO_6 octahedra for the $I4_1/acd$ and *Acam* phases rotate in opposite directions; and (b) schematic representation of the identical structural region of the $I4_1/acd$ and the *Acam* phases that display a radius of ≈ 8 Å from the probing ^{111}Cd isotope.

[1] J. P. Attfield, Frontiers Chem. **6** (2018).

[2] K. Takenaka, Frontiers Chem. **6** (2018).

[3] M. S. Senn, C. A. Murray, X. Luo, L. Wang, F.-T. Huang, S.-W. Cheong, A. Bombardi, C. Ablitt, A. A. Mosto, and N. C. Bristowe (2016).

[4] C. Ablitt, S. Craddock, M. S. Senn, A. A. Mostofi, and N. C. Bristowe, npj Comput. Mater. **3**, 44 (2017).

[5] C. Ablitt, H. McCay, S. Craddock, L. Cooper, E. Reynolds, A. A. Mostofi, N. C. Bristowe, C. A. Murray, and M. S. Senn, Chem. Mater. **32**, 605 (2020).

[6] C. Ablitt, A. A. Mostofi, N. C. Bristowe, M. S. Senn, and A. Sanson, Frontiers Chem. **6**, 1 (2018).

[7] W.-T. Chen, C. Ablitt, N. C. Bristowe, A. A. Mostofi, T. Saito, Y. Shimakawa, and M. S. Senn, Chem. Commun. **55**, 2984 (2019).

[8] C. Ablitt, M. S. Senn, and N. C. Bristowe arXiv:1810.02697.

[9] C. Ablitt, M. S. Senn, and N. C. Bristowe. J. Takahashi and N. Kamegashira, Mater. Res. Bull. **28**, 565 (1993).

[10] B. Ranjbar and B. J. Kennedy, Solid State Sci. **49**, 43 (2015).

[11] S. Yoshida, H. Akamatsu, R. Tsuji, O. Hernandez, H. Padmanabhan, A. Sen Gupta, A. S. Gibbs, K. Mibu, S. Murai, J. M. Rondinelli *et al.*, J. Am. Chem. Soc. **140**, 15690 (2018).

[12] C. Autret, C. Martin, M. Hervieu, R. Retoux, B. Raveau, G. Andre, and F. Boure, J. Solid State Chem. **177**, 2044 (2004).

[13] P. Rocha-Rodrigues, S. S. M. Santos, I. P. Miranda, G. N. P. Oliveira, J. G. Correia, L. V. C. Assali, H. M. Petrilli, J. P. Araújo, and A. M. L. Lopes, Phys. Rev. B **101**, 064103 (2020).

[14] G. N. P. Oliveira, R. C. Teixeira, R. P. Moreira, J. G. Correia, J. P. Araújo, and A. M. L. Lopes, Nat. Sci. Rep. (2020).

[15] G. Schatz and A. Weidinger, *Nuclear Condensed Matter Physics: Nuclear Methods and Applications* (Wiley, New York, 1996).

[16] J. Rodríguez-Carvajal, Physica B: Condens. Matter **192**, 55 (1993).

[17] K. Momma and F. Izumi, J. Appl. Crystallogr. **44**, 1272 (2011).

[18] A. M. L. Lopes, J. P. Araújo, E. Rita, J. G. Correia, V. S. Amaral, Y. Tomioka, Y. Tokura, and R. Suryanarayanan, J. Magn. Magn. Mater. **272-276**, E1667 (2004).

[19] A. M. L. Lopes, J. P. Araújo, J. J. Ramasco, V. S. Amaral, R. Suryanarayanan, and J. G. Correia, Phys. Rev. B **73**, 100408(R) (2006).

[20] J. G. Correia, Tech. Rep., DETN-C2TN-IST, ULisboa (2018).

[21] N. P. Barradas, Tech. Rep., ULisboa (1992).

[22] N. P. Barradas, M. Rots, A. A. Melo, and J. C. Soares, Phys. Rev. B **47**, 8763 (1993).

[23] A. M. L. Lopes, J. P. Araújo, V. S. Amaral, J. G. Correia, Y. Tomioka, and Y. Tokura, Phys. Rev. Lett. **100**, 155702 (2008).

[24] D. J. Singh, *Planewaves, Pseudopotentials and the LAPW Method* (Springer US, Boston, MA, 1994).

[25] K. Schwarz and P. Blaha, Comput. Mater. Sci. **28**, 259 (2003), proceedings of the Symposium on Software Development for Process and Materials Design.

[26] P. Hohenberg and W. Kohn, Phys. Rev. **136**, B864 (1964).

[27] W. Kohn and L. J. Sham, Phys. Rev. **140**, A1133 (1965).

[28] J. P. Perdew, K. Burke, and M. Ernzerhof, Phys. Rev. Lett. **77**, 3865 (1996).

[29] H. J. Monkhorst and J. D. Pack, Phys. Rev. B **13**, 5188 (1976).

[30] B. J. Campbell, H. T. Stokes, D. E. Tanner, and D. M. Hatch, J. Appl. Crystallogr. **39**, 607 (2006).

[31] H. T. Stokes, D. M. Hatch, and B. J. Campbell, ISOTROPY Software Suite.

[32] P. Giannozzi, O. Andreussi, T. Brumme, O. Bunau, M. B. Nardelli, M. Calandra, R. Car, C. Cavazzoni, D. Ceresoli, M. Cococcioni *et al.*, J. Phys.: Condens. Matter **29**, 465901 (2017).

[33] P. Giannozzi, S. Baroni, N. Bonini, M. Calandra, R. Car, C. Cavazzoni, D. Ceresoli, G. L. Chiarotti, M. Cococcioni, I. Dabo *et al.*, J. Phys.: Condens. Matter **21**, 395502 (2009).

[34] P. E. Blöchl, Phys. Rev. B **50**, 17953 (1994).

[35] N. A. Benedek and C. J. Fennie, Phys. Rev. Lett. **106**, 107204 (2011).

[36] S. Matar, M. Subramanian, and R. Weihrich, Chem. Phys. **310**, 231 (2005).

[37] M. Norton, R. Tom, and W. Glaunsinger, J. Solid State Chem. **48**, 242 (1983).

[38] See the Supplemental Material at http://link.aps.org/supplemental/10.1103/PhysRevB.xx.xxxxxx for the $R(t)$ anisotropy functions measured below Ca$_2$MnO$_4$ magnetic transition and information on the refinements of the neutron diffraction profiles measured at 298 and 1223 K.

[39] T. Kushida, J. Sci. Hiroshima Univ. Series A **19**, 327 (1955).

[40] T. Kushida, G. B. Benedek, and N. Bloembergen, Phys. Rev. **104**, 1364 (1956).

[41] U. Müller, *Symmetry Relationships between Crystal Structures. Applications of Crystallographic Group Theory in Crystal Chemistry* (Oxford University Press, Oxford, 2017).